



Here we present the experimental Raman data for [6]-, [8]-, [10]-, and [12]CPPs, the smallest even-numbered carbon nanohoops synthesized to date. We compare them to the corresponding calculated Raman spectra using density functional theory (DFT). By taking advantage of group theory in these highly symmetric molecules, we are able to assign the observed Raman modes, as well as the vibrational size dependence.

## 2. EXPERIMENTAL AND COMPUTATIONAL METHODS

The samples were bulk solid CPP material prepared by drop-drying CPP/chloroform solutions on separate glass substrates and letting the chloroform evaporate completely. The Raman spectra for the [6]-, [8]-, [10]-, and [12]CPPs were acquired under ambient conditions using backscattering geometry with a  $20\times 0.4$  N.A. microscope objective and a 785 nm laser with the incident power around 0.3 mW. These Raman results were compared to low-power ( $\sim 0.01$  mW) test results of the same samples to make sure that no heating effects were present under the 0.3 mW laser power.

DFT Raman calculations for the [4]–[20] (even-numbered) CPPs were carried out using the Gaussian 09 programs<sup>24</sup> with the B3LYP exchange correlation functional and the 6-31G\* basis set. The DFT spectra were adjusted with empirical scaling factors obtained by linear regressions of the calculated and experimental peak positions.

Computational results<sup>25,26</sup> indicate that the ground-state geometries of the even-numbered [n]CPP molecules exhibit  $D_{(n/2)d}$  symmetry, for which the benzene units are alternately canted with a certain dihedral angle between adjacent units. In contrast, all of the odd-numbered CPPs are asymmetric molecules ( $C_1$  symmetry). Here we concentrate on the higher symmetry even-numbered CPPs. As shown in Figure 2a an even

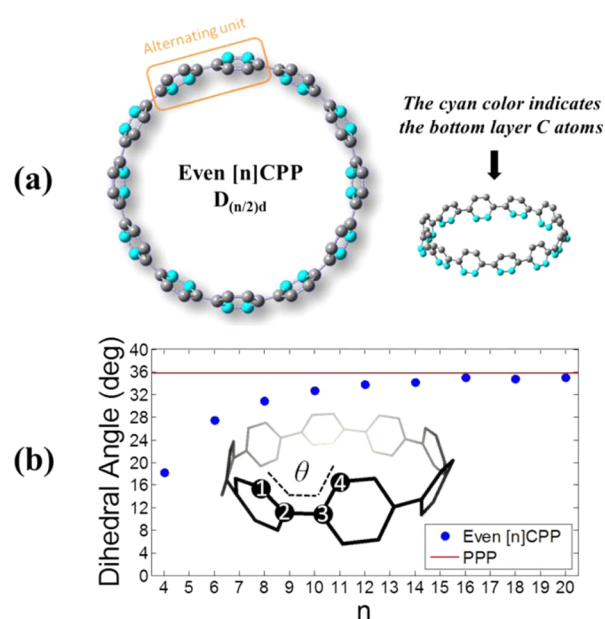


**Figure 2.** Geometries of even-numbered CPP molecules. (a) An even [n]CPP has a symmetry of  $D_{(n/2)d}$  where the benzene units are alternately canted with a certain dihedral angle between adjacent units. (b) The plot shows the size dependence of the dihedral angle. The dihedral angle  $\theta$  is the angle between the plane defined by atoms (1, 2, 3) and that by atoms (2, 3, 4). The red line ( $\sim 35.8^\circ$ ) indicates the dihedral angle of a long polyparaphenylene (PPP) molecule and is an approximation of the dihedral angle for [n]CPP when  $n \rightarrow \infty$ .

[n]CPP molecule can be viewed as a hoop with  $n/2$  repetitions of a double-benzene unit. Figure 2b shows that the dihedral angles of [n]CPPs increase with  $n$  and tend to converge to a constant value around  $35.8^\circ$ , which is the theoretical dihedral angle of a polyparaphenylene (PPP) open chain.

## 3. EXPERIMENTAL AND COMPUTATIONAL RESULTS

**3.1. Raman Spectra.** Figure 3 displays both the experimental and calculated Raman spectra for [6]-, [8]-, [10]-, and [12]CPPs. The calculated Raman peaks below  $1400\text{ cm}^{-1}$  are underestimated in amplitude for all of the CPPs. The insets in Figure 3 show the magnified low-frequency regions, from which we can also see some apparent discrepancies in the relative intensities between the experiments and calculations, for instance, the multiplex band around  $800\text{ cm}^{-1}$ , especially for the [10]- and [12]CPPs. Apart from the relative intensity issue, the corresponding experimental and theoretical results agree well with each other.

**3.2. Irreducible Representations of the Raman Modes.** Table 1 lists the Raman-active modes for even [n]CPPs from our group theory calculations. Generally, for even-numbered CPPs with  $D_{(n/2)d}$  point group symmetry, there are 133 Raman modes ( $15A_1 + 30E_2 + 29E_{n/2-1}$ , when  $n/2$  is even, and  $15A_{1g} + 29E_{1g} + 30E_{2g}$ , when  $n/2$  is odd). Two exceptions are [4]- and [6]CPPs, the smallest possible even-numbered carbon nanohoops, where [4]CPP has 100 Raman modes ( $15A_1 + 15B_1 + 14B_2 + 28E$ ) and [6]CPP has 73 ( $15A_{1g} + 29E_g$ ) due to their lower symmetries and degrees of freedom. Our predictions of the number of the modes and their symmetries are in accordance with the results from the DFT computations for all carbon nanohoops from [4]- to [20]CPPs. The calculations show that there are a dense number of modes up to  $\sim 1800\text{ cm}^{-1}$ , followed by a gap until  $\sim 3000\text{ cm}^{-1}$ . The modes above  $3000\text{ cm}^{-1}$  are related to the C–H bond stretching.<sup>26</sup> Here we confine our experimental measurements, and thus theoretical discussions, only to the modes below  $1800\text{ cm}^{-1}$ .

## 4. ANALYSIS AND DISCUSSION

**4.1. High-Frequency Regime ( $\sim 1150\text{--}1700\text{ cm}^{-1}$ ).** We show in Figure 4 the frequency region  $1450\text{--}1650\text{ cm}^{-1}$  of the experimental Raman spectra for the four CPPs. The three significant peaks observed are attributable to the carbon–carbon bond stretching. The peak around  $1500\text{ cm}^{-1}$  is a doubly degenerate mode, with the irreducible representation  $E_g$  for [6]CPP,  $E_{2g}$  for [10]CPP (and larger even-numbered [n]CPPs when  $n/2$  is odd), and  $E_2$  for [8]- and [12]CPPs (and larger even-numbered [n]CPPs when  $n/2$  is even). We name it the  $G_{10}$  mode as it corresponds to the  $C_{\text{ipso}}\text{--}C_{\text{ortho}}$  bond stretch. The peak with the highest intensity (namely, the  $G_1$  mode) is a totally symmetric mode ( $A_1$  when  $n/2$  is even, and  $A_{1g}$  when  $n/2$  is odd, which we will denote collectively as  $A_{1(g)}$ ) for all even-numbered [n]CPPs. The side peak to the right of  $G_1$  is a doubly degenerate mode, which we call the  $G_2$  mode. Similar to the  $G_{10}$  mode,  $G_2$  is  $E_g$  for [6]CPP,  $E_{2g}$  for [10]CPP (and larger even-numbered [n]CPPs when  $n/2$  is odd), and  $E_2$  for [8]- and [12]CPPs (and larger even-numbered [n]CPPs when  $n/2$  is even). We shall denote  $E_2$  and  $E_{2g}$  as  $E_{2(g)}$  collectively for the following discussion. Both the  $G_1$  and  $G_2$  modes are related to the  $C_{\text{ortho}}\text{--}C_{\text{ortho}}$  and  $C_{\text{ipso}}\text{--}C_{\text{ipso}}$  bond stretching. The nomenclature  $G_1$ ,  $G_2$ , and  $G_{10}$  is chosen to emphasize the kinship with the G modes of CNTs and graphene corresponding to the C atom vibrations tangential to the surface.<sup>26–28</sup> As  $n$  increases, the  $G_{10}$

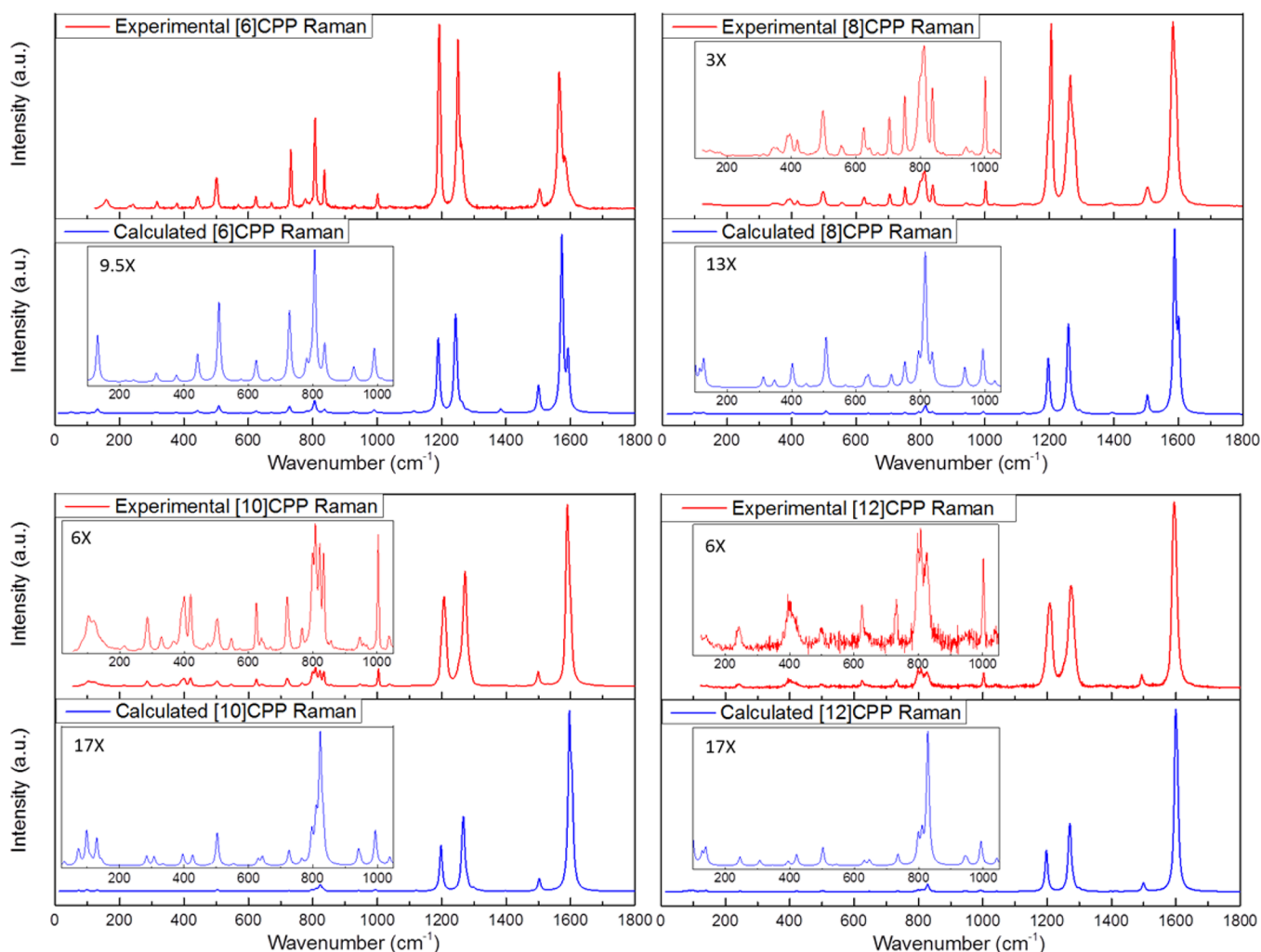


**Figure 3.** Experimental (red) and calculated (blue) Raman spectra for [6]-, [8]-, [10]-, and [12]CPPs. A universal scaling factor of 0.97 is used to scale the original calculated frequencies of all CPPs. The insets magnify the low-frequency regions in which the Raman amplitudes are small. Comparisons of the experimental and calculated spectra show high agreement between one another except for some apparent differences in the relative intensities.

**Table 1. Theoretical Raman-Active Modes for Even-Numbered [n]CPPs<sup>a</sup>**

	Raman-Active Modes	Special Cases
$n/2$ is even	$15A_1 + 30E_2 + 29E_{n/2-1}$ (133 modes)	$15A_1 + 15B_1 + 14B_2 + 28E$ for $n = 4$ (100 modes)
$n/2$ is odd	$15A_1 + 29E_{1g} + 30E_{2g}$ (133 modes)	$15A_1 + 29E_g$ for $n = 6$ (73 modes)

<sup>a</sup>A, B – single modes; E – doubly-degenerate modes.

mode decreases in frequency, whereas both the  $G_1$  and  $G_2$  modes increase in frequency with a decreasing separation between them. Our calculations show that the  $C_{\text{ipso}}-C_{\text{ipso}}$  bonds exhibit more single-bond character with decreasing  $n$ , as indicated by the increasing bond lengths. Such weakening of the  $C_{\text{ipso}}-C_{\text{ipso}}$  bonds due to increasing strain (as  $n$  decreases) is also associated with relative strengthening of the  $C_{\text{ipso}}-C_{\text{ortho}}$  bonds, thus giving rise to the decrease in  $G_1$  and  $G_2$  frequencies and the increase in  $G_{10}$  frequency (as  $n$  decreases). The reader is directed to ref 26 for more information on the size dependence of the CPP G modes. Fitted experimental Raman frequencies for the G peaks, as well as various other peaks, of [6]-, [8]-, [10]-, and [12]CPPs can be found in the Supporting Information.

The two bands around 1200 and 1275  $\text{cm}^{-1}$  in Figure 5 are related to the C–H bond bending in the benzene planes and the breathing (or irregular deformations) of the benzene units, respectively. Specifically, the peaks in the 1200  $\text{cm}^{-1}$  band correspond to C–H bending motions where the intrabenzene H atoms move against each other, as exemplified by the strongest  $A_1$  mode ( $\sim 1200 \text{ cm}^{-1}$ ) in this band for [8]CPP; the peaks in the 1275  $\text{cm}^{-1}$  band are related to the asymmetric breathing or irregular in-plane distortions of the six-member carbon rings, with the strongest peak representing a totally symmetric mode (e.g.,  $A_1$  around 1270  $\text{cm}^{-1}$  for [8]CPP in Figure 5). We relate the 1275  $\text{cm}^{-1}$  band to the D-band in CNTs because of their similar six-carbon-ring behaviors and comparable frequency regions,<sup>21,29–31</sup> except that the momentum conservation requirement in solid state CNTs is relaxed for CPPs due to their molecular nature; hence, they are allowed without defects. In fact, this band is prominent in CPPs. As is seen in Figure 5, the most intense peaks in these two bands for the even-numbered CPPs are both totally symmetric modes  $A_{1(g)}$ . Figure 6 shows the overlaid comparisons of the experimental and calculated Raman spectra for the four CPP species. We have scaled the frequencies (for typically  $\sim \pm 5\%$ ) of the original calculated Raman spectra for each individual CPP so that the two strongest modes in the

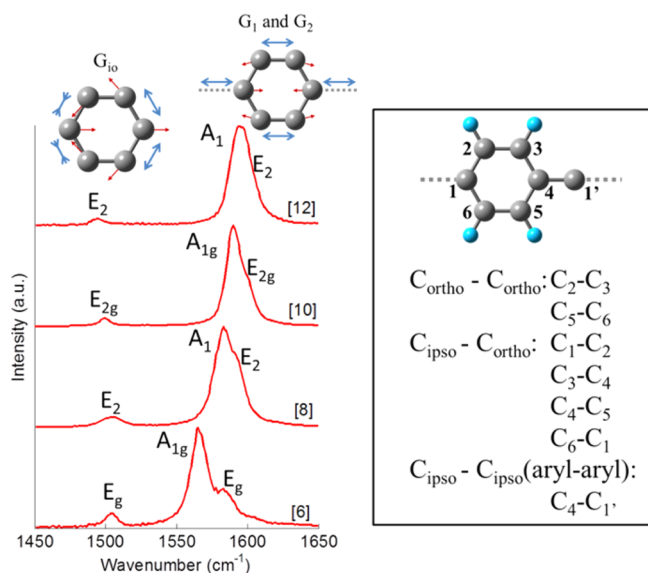


**Figure 4.** Experimental Raman spectra in the high-frequency region 1450–1650  $\text{cm}^{-1}$ . The  $G_{10}$  mode corresponds to  $C_{\text{ippo}}-C_{\text{ortho}}$  bond stretch, and the  $G_1$  and  $G_2$  modes correspond to  $C_{\text{ippo}}-C_{\text{ippo}}$  and  $C_{\text{ortho}}-C_{\text{ortho}}$  bond stretch. As  $n$  increases, the  $G_{10}$  mode decreases in frequency, whereas the  $G_1$  and  $G_2$  modes increase with a decreasing separation between one another.

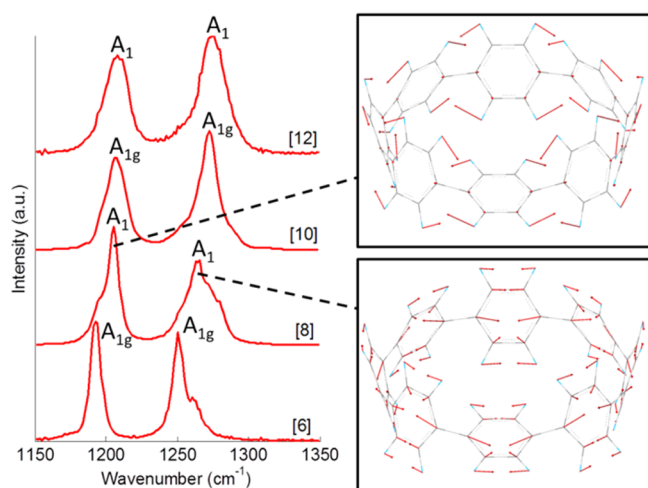


**Figure 5.** Experimental Raman spectra between 1150 and 1350  $\text{cm}^{-1}$ . The 1200  $\text{cm}^{-1}$  band corresponds to C–H bending motions where the intrabenzene H atoms move against each other. The peaks in the 1275  $\text{cm}^{-1}$  band are related to the asymmetric breathing or irregular in-plane distortions of the six-member carbon rings. The most intense peaks in these two bands for the even-numbered CPPs are both totally symmetric modes  $A_1$  or  $A_{1g}$ .

scaled spectra overlap with the maxima of the experimental peaks. The theoretical Raman-active modes are marked as the blue matchsticks and denoted with their corresponding irreducible representations. The symmetries of the observed side peaks in these two bands cannot be determined conclusively from the calculated spectra. It would require polarization analysis to do so irrefutably. Nevertheless, we are still able to make some general comments about these modes based on symmetry: (1) The side peaks to the left of the  $A_{1(g)}$  mode in the 1200  $\text{cm}^{-1}$  band may arise from doubly degenerate modes. For [6]CPP, the only possibility is the  $E_g$  mode according to the DFT calculation;

for other even-numbered  $[n]$ CPP with odd  $n/2$ , there can be two contributing modes,  $E_{1g}$  and  $E_{2g}$ , as shown for [10]CPP in Figure 6; for even  $[n]$ CPP where  $n/2$  is even, there are also two possible modes,  $E_2$  and  $E_{n/2-1}$ , for example,  $E_2$  and  $E_3$  for [8]CPP and  $E_2$  and  $E_5$  for [12]CPP. It is worth noting that even though some of the modes are predicted to be insignificant in intensity, they may still be visible in experiment owing to either symmetry breaking or overall inaccuracy in the calculated intensities.<sup>32</sup> (2) The side peaks around the  $A_{1(g)}$  mode in the 1275  $\text{cm}^{-1}$  band may also arise from the doubly degenerate modes. For [6]CPP, there are two  $E_g$  modes on the right side of the  $A_{1g}$  peak; for other even  $[n]$ CPP where  $n/2$  is odd, starting from [10]CPP, there are two  $E_{1g}$  modes and two  $E_{2g}$  modes close to the  $A_{1g}$  peak; similarly, for even  $[n]$ CPP where  $n/2$  is even, there are two  $E_2$  modes and two  $E_{n/2-1}$  modes. (3) In the right tail of the 1275  $\text{cm}^{-1}$  band one may observe small signals from an  $A_{1(g)}$  mode and several doubly degenerate modes. (4) It is also possible that the discrepancies between the calculated and observed peak positions, for example, the experimental peaks to the right of the 1250  $\text{cm}^{-1}$   $A_{1g}$  peak for [6]CPP, result from imprecise calculation in DFT<sup>32</sup> or from symmetry breaking and the concomitant peak shift in the real-world measurements.

**4.2. Intermediate-Frequency Regime ( $\sim 530$ – $1150 \text{ cm}^{-1}$ ).** It can be seen from Figure 3 that the experimental Raman peaks below 1150  $\text{cm}^{-1}$  are generally low in intensity. The only significant peak in the frequency regime 900–1150  $\text{cm}^{-1}$  is around 1000  $\text{cm}^{-1}$  from a doubly degenerate mode  $E_{2(g)}$  (or  $E_g$  for [6]CPP) as shown in Figure 7. In Figure 7 we use [8]CPP to illustrate that the vibrational motion of the modes are composed of two benzene vibrational modes: a Raman-active mode and a Raman-inactive mode corresponding to two types of six-member carbon rings breathing with constant C–H bond lengths, both around 990  $\text{cm}^{-1}$  in the benzene Raman spectrum.

In Figure 8, the significant modes are highlighted and grouped according to their vibrational motions and symmetries. Using the symmetry arguments, we are able to identify the size dependence of various modes in this regime. Groups a–d are all composed of doubly degenerate modes of irregular bond bending and/or ring deformations. There are several closely spaced modes in group b with various relative intensities for different CPPs, and we are unable to assign the irreducible representations to each of them with confidence at the time. Representative modes for the four groups are laid out on top of Figure 8. Group e in the trapezoidal area defines a special category of CPP Raman-active modes that are characterized by out-of-plane C–H bond bending motions. Figure 9 is a magnification of the regime (780–850  $\text{cm}^{-1}$ ) where the strongest of these modes reside. Although considerable discrepancies in relative intensities exist between the experiments and the calculations, the comparison still provides enough insight in the positions of the peaks. The four most important peaks are the three  $A_{1(g)}$  modes and the doubly degenerate mode on the right tail, examples of which are taken from the [8]CPP calculations.

**4.3. Low-Frequency Regime (below 530  $\text{cm}^{-1}$ ).** The low-frequency peaks below 530  $\text{cm}^{-1}$  are very weak and almost negligible compared to the high-energy peaks, which can be observed in both the experimental and calculated spectra in Figure 3. We exhibit in Figure 10 the lowest frequency part of our measured Raman spectra. Signals around and below 150  $\text{cm}^{-1}$  are questionable, as they may be polluted by signal from the laser. Theoretically, the peaks below 200  $\text{cm}^{-1}$  mostly come from vibrations of the atoms in the radial direction of the hoop such as radial breathing modes (RBMs) and squeezing modes, which are

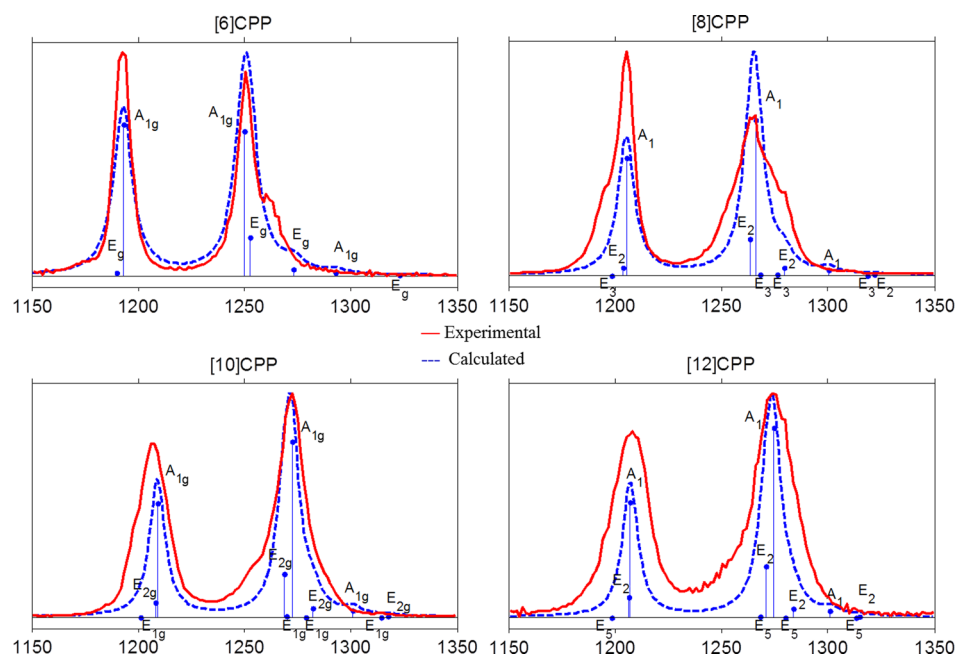


**Figure 6.** Comparisons between the experimental and calculated Raman spectra in the region between 1150 and 1350  $\text{cm}^{-1}$ . We scaled the original calculated Raman spectra for each individual CPP so that the two strongest modes in the scaled spectra overlap with the maxima of the experimental peaks. Separate scaling factors (0.972, 0.977, 0.978, and 0.977 for [6]-, [8]-, [10]-, and [12]CPPs, respectively) are used for optimal overlap of the experimental and calculated peaks. The theoretical Raman-active modes are marked as the blue matchsticks and denoted with their corresponding irreducible representations. Side peaks in these two bands may arise from various doubly degenerate modes.

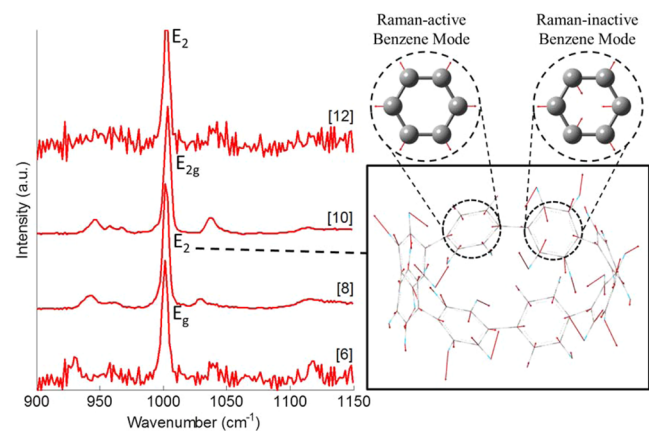


**Figure 7.** Peak around 1000  $\text{cm}^{-1}$  ( $E_g$  for [6]CPP;  $E_{2g}$  for other even [n]CPPs with  $n/2$  being odd;  $E_2$  for even [n]CPPs with  $n/2$  being even) is due to the vibrational modes composed of two types of benzene vibrational modes. The mode in the left inset is an active mode in the Raman spectrum of benzene, and the one in the right inset, inactive. Both benzene modes are around 990  $\text{cm}^{-1}$ .

also present in CNTs.<sup>33,34</sup> The modes between 200 and 450  $\text{cm}^{-1}$  can be roughly characterized as vibrations with minimal intrabenzene bond length change. Of particular interest in this area is the single peak ( $A_{1(g)}$ ) around 500  $\text{cm}^{-1}$ , named the radial flexing mode (RFM) because of the synchronous flexing motions of all the benzene units in the hoop radial direction.<sup>26</sup> Like the RBM for CNTs, the radial flexing mode is dependent on the size of the nanohoop, but it is distinct from the RBM in that the RBM corresponds to the expansion–contraction motion of the tube in the radial direction.<sup>35,36</sup> While the RBM serves as the signature Raman mode of CNTs, which is extensively used for the identification of nanotube species due to its size dependence effect, the radial flexing mode may be of less

importance to the CPPs because of its low intensity and, more importantly, the fact that all of the CPP Raman modes are more or less size dependent.

**4.4. Size Dependence of the CPP Raman Modes.** Figure 11 displays the size dependence of selected calculated Raman frequencies between 0 and 1600  $\text{cm}^{-1}$ . At the top of the figure, we use the experimental Raman spectrum of [8]CPP as a sample to show the approximate positions of different modes. The filled circles (blue) indicate the five most significant modes in the high-frequency regime as discussed in section 4.1, including the G modes and the strongest modes in the 1200  $\text{cm}^{-1}$  band and the 1275  $\text{cm}^{-1}$  band (D band), respectively. The empty circles (green) indicate the two significant modes in the intermediate regime as discussed in section 4.2, including the strongest mode in the 800  $\text{cm}^{-1}$  band and the 1000  $\text{cm}^{-1}$  mode. The empty squares (red) indicate selected modes in the low-frequency regime, including the radial flexing mode discussed in section 4.3 and three other insignificant modes. All points are labeled with their irreducible representations. Note that due to the lower symmetry of [4]CPP, some of its Raman modes bear different representations than the larger CPPs. All modes shown in the plot are size dependent for  $n \leq 14$ , but tend to converge to certain constant values as  $n$  becomes large, a behavior similar to that of the size dependence of the dihedral angle shown in Figure 2b. Similar to the convergence of the dihedral angle, the Raman frequencies should also converge to their limiting values defined by the Raman-active modes of the linear PPP molecule. It is worth noting that the calculated Raman frequencies shown in Figure 11 (as well as the calculated Raman spectra and modes shown in all previous figures) are scaled from the original calculated Raman spectra by DFT. The original calculated Raman frequencies are in general higher than the experimental values. This overestimation is a common problem for the DFT Raman spectra of large molecular systems and is likely caused by



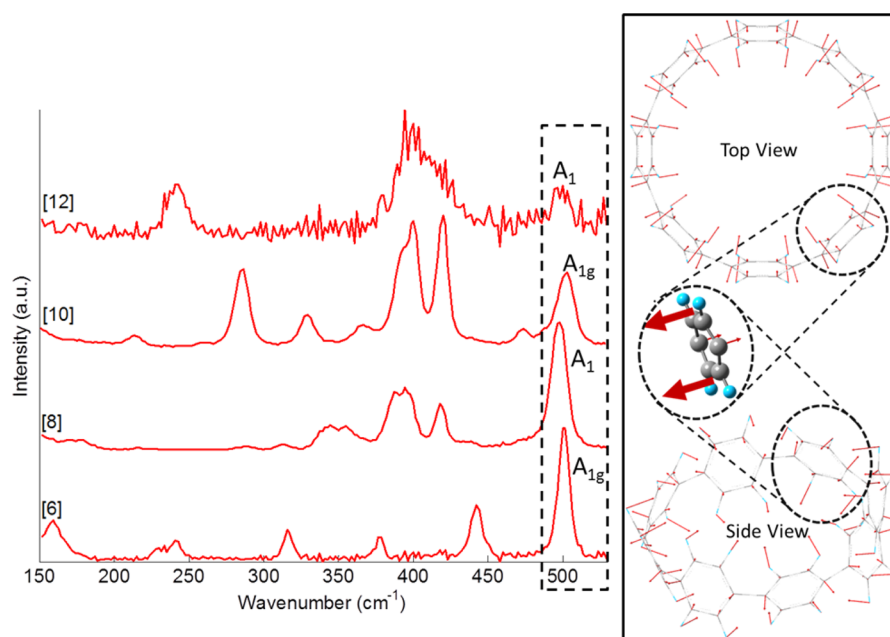


**Figure 10.** Low-frequency region ( $<500\text{ cm}^{-1}$ ) for [6]-, [8]-, [10]-, and [12]CPPs. Peaks in this region have very low intensities compared to the high-frequency peaks. The single peak around  $500\text{ cm}^{-1}$  corresponds to a totally symmetric mode in which all of the benzene units synchronously flex in the radial direction of the hoop.

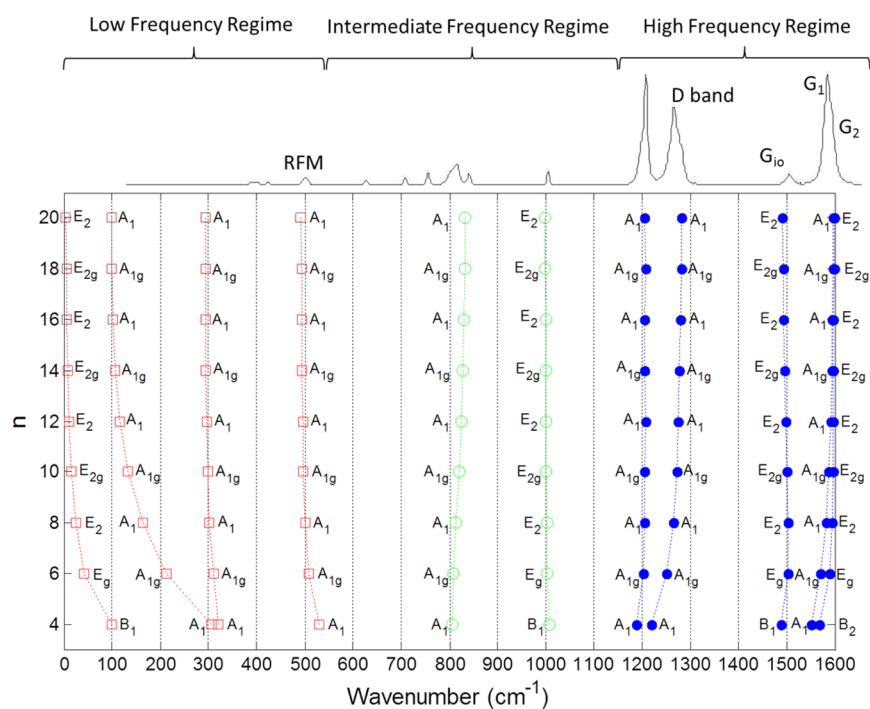


**Figure 11.** Size dependence of selected calculated Raman frequencies of even-numbered CPPs. A universal scaling factor of 0.97 is used. The sample spectrum on top is the experimental Raman spectrum from [8]CPP. The filled circles (blue) indicate the five most significant modes in the high-frequency regime as discussed in section 4.1, including the G modes and the strongest modes in the  $1200\text{ cm}^{-1}$  band and  $1275\text{ cm}^{-1}$  band (D band), respectively; the empty circles (green) indicate the two significant modes in the intermediate regime as discussed in section 4.2; the empty squares (red) indicate selected modes in the low-frequency regime, including the radial flexing mode discussed in section 4.3 and three other insignificant modes. All points are labeled with their respective symmetries. As  $n$  becomes large, all modes tend to converge to the limit values defined by the infinite PPP molecule.

## 5. CONCLUSION

We have analyzed the Raman spectra of [6]-, [8]-, [10]-, and [12]CPPs with the help of DFT calculations and group theory. The total numbers of Raman-active modes for even  $[n]$ CPPs with  $D_{(n/2)d}$  symmetries are predicted by group theory and

confirmed by comparisons with the DFT results. Key Raman-active modes of even-numbered CPPs are discussed in detail, and all major peaks are categorized according to their vibrational motions and/or point group. By taking advantage of the symmetry arguments, we are able to identify both experimental

and calculated Raman modes of the same origin in different CPPs and thus to observe their size dependency. These will be useful in studying the evolution from the CPP Raman modes to the CNT Raman modes, to bridge the gap between the Raman spectroscopies of the carbon nanohoops and nanotubes. In addition, the group theory of ground-state even-numbered CPPs may also serve as a useful baseline for probing any symmetry-breaking effects in CPPs due to strain or vibronic coupling.

## ■ ASSOCIATED CONTENT

### ● Supporting Information

Fitted values for selected experimental Raman frequencies of [6]-, [8]-, [10]-, and [12]CPPs; theoretical vibrational modes, and optimized Cartesian coordinates of ground-state even [*n*]CPPs. This material is available free of charge via the Internet at <http://pubs.acs.org>.

## ■ AUTHOR INFORMATION

### Corresponding Authors

\*(H.C.) E-mail: [chenhang@bu.edu](mailto:chenhang@bu.edu).

\*(A.K.S.) E-mail: [swan@bu.edu](mailto:swan@bu.edu).

### Present Address

<sup>Δ</sup>Department of Chemistry and Biochemistry and Materials Science Institute, University of Oregon, Eugene, OR 97403, USA.

### Notes

The authors declare no competing financial interest.

## ■ ACKNOWLEDGMENTS

H.C. and A.K.S. acknowledge support from Boston University College of Engineering. M.R.G. and R.J. acknowledge the National Science Foundation (CHE-1255219), and M.R.G. thanks Vertex Pharmaceuticals for a graduate research fellowship. F.W. acknowledges support from the Arkansas Biosciences Institute. S.K.D. and S.T. acknowledge partial support of the LANL LDRD program. This work was performed in part at the Center for Integrated Nanotechnologies, a U.S. Department of Energy, Office of Basic Energy Sciences user facility.

## ■ REFERENCES

- (1) Jasti, R.; Bhattacharjee, J.; Neaton, J. B.; Bertozzi, C. R. Synthesis, Characterization, and Theory of [9]-, [12]-, and [18]-Cycloparaphenylene: Carbon Nanohoop Structures. *J. Am. Chem. Soc.* **2008**, *130*, 17646–17647.
- (2) Fort, E. H.; Scott, L. T. One-Step Conversion of Aromatic Hydrocarbon Bay Regions into Unsubstituted Benzene Rings: A Reagent for the Low-Temperature, Metal-Free Growth of Single-Chirality Carbon Nanotubes. *Angew. Chem., Int. Ed.* **2010**, *49*, 6626–6628.
- (3) Fort, E. H.; Scott, L. T. Carbon Nanotubes from Short Hydrocarbon Templates. Energy Analysis of the Diels-Alder Cycloaddition/Rearomatization Growth Strategy. *J. Mater. Chem.* **2011**, *21*, 1373–1381.
- (4) Omachi, H.; Nakayama, T.; Takahashi, E.; Segawa, Y.; Itami, K. Initiation of Carbon Nanotube Growth by Well-defined Carbon Nanorings. *Nat. Chem.* **2013**, *5*, 572–576.
- (5) Segawa, Y.; Senel, P.; Matsuura, S.; Omachi, H.; Itami, K. [9]Cycloparaphenylene: Nickel-mediated Synthesis and Crystal Structure. *Chem. Lett.* **2011**, *40*, 423–425.
- (6) Segawa, Y.; Miyamoto, S.; Omachi, H.; Matsuura, S.; Senel, P.; Sasamori, T.; Tokitoh, N.; Itami, K. Concise Synthesis and Crystal Structure of [12]Cycloparaphenylene. *Angew. Chem., Int. Ed.* **2011**, *50*, 3244–3248.

(7) Yamago, S.; Watanabe, Y.; Iwamoto, T. Synthesis of [8]-Cycloparaphenylene from a Square-Shaped Tetranuclear Platinum Complex. *Angew. Chem., Int. Ed.* **2010**, *49*, 757–759.

(8) Omachi, H.; Matsuura, S.; Segawa, Y.; Itami, K. A Modular and Size-Selective Synthesis of [*n*]Cycloparaphenylenes: A Step toward the Selective Synthesis of (*n*, *n*) Single-Walled Carbon Nanotubes. *Angew. Chem., Int. Ed.* **2010**, *49*, 10202–10205.

(9) Iwamoto, T.; Watanabe, Y.; Sakamoto, Y.; Suzuki, T.; Yamago, S. Selective and Random Syntheses of [*n*]Cycloparaphenylenes (*n* = 8–13) and Size Dependence of Their Electronic Properties. *J. Am. Chem. Soc.* **2011**, *133*, 8354–8361.

(10) Sisto, T. J.; Golder, M. R.; Hirst, E. S.; Jasti, R. Selective Synthesis of Strained [7]Cycloparaphenylene: An Orange-Emitting Fluorophore. *J. Am. Chem. Soc.* **2011**, *133*, 15800–15802.

(11) Darzi, E. R.; Sisto, T. J.; Jasti, R. Selective Syntheses of [7]-[12]Cycloparaphenylenes Using Orthogonal Suzuki-Miyaura Cross-Coupling Reactions. *J. Org. Chem.* **2012**, *77*, 6624–6628.

(12) Xia, J. L.; Bacon, J. W.; Jasti, R. Gram-Scale Synthesis and Crystal Structures of [8]- and [10]CPP, and the Solid-State Structure of C-60@[10]CPP. *Chem. Sci.* **2012**, *3*, 3018–3021.

(13) Xia, J.; Jasti, R. Synthesis, Characterization, and Crystal Structure of [6]Cycloparaphenylene. *Angew. Chem., Int. Ed.* **2012**, *51*, 2474–2476.

(14) Iwamoto, T.; Watanabe, Y.; Sadahiro, T.; Haino, T.; Yamago, S. Size-Selective Encapsulation of C-60 by [10]Cycloparaphenylene: Formation of the Shortest Fullerene-Peapod. *Angew. Chem., Int. Ed.* **2011**, *50*, 8342–8344.

(15) Zabula, A. V.; Filatov, A. S.; Xia, J. L.; Jasti, R.; Petrukhina, M. A. Tightening of the Nanobelt upon Multielectron Reduction. *Angew. Chem., Int. Ed.* **2013**, *52*, 5033–5036.

(16) Golder, M. R.; Wong, B. M.; Jasti, R. Photophysical and Theoretical Investigations of the [8]Cycloparaphenylene Radical Cation and Its Charge-Resonance Dimer. *Chem. Sci.* **2013**, *4*, 4285–4291.

(17) Hirst, E. S.; Jasti, R. Bending Benzene: Syntheses of [*n*]Cycloparaphenylenes. *J. Org. Chem.* **2012**, *77*, 10473–10478.

(18) Adamska, L.; Nayyar, I.; Chen, H.; Swan, A.; Oldani, N.; Fernandez-Alberti, S.; Golder, M.; Jasti, R.; Doorn, S.; Tretiak, S. Self-Trapping of Excitons, Violation of Condon Approximation and Efficient Fluorescence in Conjugated Cycloparaphenylenes. *Nano Lett.* **2014**, *14*, 6539–6546.

(19) Steinberg, B. D.; Scott, L. T. New Strategies for Synthesizing Short Sections of Carbon Nanotubes. *Angew. Chem., Int. Ed.* **2009**, *48*, 5400–5402.

(20) Jasti, R.; Bertozzi, C. R. Progress and Challenges for the Bottom-up Synthesis of Carbon Nanotubes with Discrete Chirality. *Chem. Phys. Lett.* **2010**, *494*, 1–7.

(21) Dresselhaus, M. S.; Jorio, A.; Hofmann, M.; Dresselhaus, G.; Saito, R. Perspectives on Carbon Nanotubes and Graphene Raman Spectroscopy. *Nano Lett.* **2010**, *10*, 751–758.

(22) Saito, R.; Hofmann, M.; Dresselhaus, G.; Jorio, A.; Dresselhaus, M. S. Raman Spectroscopy of Graphene and Carbon Nanotubes. *Adv. Phys.* **2011**, *60*, 413–550.

(23) Duque, J. G.; Chen, H.; Swan, A. K.; Shreve, A. P.; Kilina, S.; Tretiak, S.; Tu, X.; Zheng, M.; Doorn, S. K. Violation of the Condon Approximation in Semiconducting Carbon Nanotubes. *ACS Nano* **2011**, *5*, 5233–5241.

(24) Frisch, M. J.; Trucks, G. W.; Schlegel, H. B.; Scuseria, G. E.; Robb, M. A.; Cheeseman, J. R.; Scalmani, G.; Barone, V.; Mennucci, B.; Petersson, G. A.; et al. *Gaussian 09*; Gaussian, Inc.: Wallingford, CT, USA, 2009.

(25) Segawa, Y.; Omachi, H.; Itami, K. Theoretical Studies on the Structures and Strain Energies of Cycloparaphenylenes. *Org. Lett.* **2010**, *12*, 2262–2265.

(26) Chen, H.; Golder, M. R.; Wang, F.; Jasti, R.; Swan, A. K. Raman Spectroscopy of Carbon Nanohoops. *Carbon* **2014**, *67*, 203–213.

(27) Pimenta, M. A.; Marucci, A.; Empedocles, S. A.; Bawendi, M. G.; Hanlon, E. B.; Rao, A. M.; Eklund, P. C.; Smalley, R. E.; Dresselhaus, G.; Dresselhaus, M. S. Raman Modes of Metallic Carbon Nanotubes. *Phys. Rev. B* **1998**, *58*, 16016–16019.

(28) Haroz, E. H.; Duque, J. G.; Tu, X.; Zheng, M.; Walker, A. R. H.; Hauge, R. H.; Doorn, S. K.; Kono, J. Fundamental Optical Processes in Armchair Carbon Nanotubes. *Nanoscale* **2013**, *5*, 1411–1439.

(29) Tuinstra, F.; Koenig, J. L. Raman Spectrum of Graphite. *J. Chem. Phys.* **1970**, *53*, 1126–1130.

(30) Ferrari, A. C.; Robertson, J. Interpretation of Raman Spectra of Disordered and Amorphous Carbon. *Phys. Rev. B* **2000**, *61*, 14095–14107.

(31) Ferrari, A. C. Raman Spectroscopy of Graphene and Graphite: Disorder, Electron-phonon Coupling, Doping and Nonadiabatic Effects. *Solid State Commun.* **2007**, *143*, 47–57.

(32) Krishnakumar, V.; Prabavathi, N. Simulation of IR and Raman Spectral Based on Scaled DFT Force Fields: A Case Study of 2-amino 4-hydroxy 6-trifluoromethylpyrimidine, with Emphasis on Band Assignment. *Spectrochim. Acta, Part A* **2008**, *71*, 449–457.

(33) Eklund, P. C.; Holden, J. M.; Jishi, R. A. Vibrational Modes of Carbon Nanotubes: Spectroscopy and Theory. *Carbon* **1995**, *33*, 959–972.

(34) Kahn, D.; Lu, J. P. Vibrational Modes of Carbon Nanotubes and Nanoropes. *Phys. Rev. B* **1999**, *60*, 6535–6540.

(35) Dresselhaus, M. S.; Dresselhaus, G.; Saito, R.; Jorio, A. Raman Spectroscopy of Carbon Nanotubes. *Phys. Rep.* **2005**, *409*, 47–99.

(36) Araujo, P. T.; Maciel, I. O.; Pesce, P. B. C.; Pimenta, M. A.; Doorn, S. K.; Qian, H.; Hartschuh, A.; Steiner, M.; Grigorian, L.; Hata, K.; Jorio, A. Nature of the Constant Factor in the Relation Between Radial Breathing Mode Frequency and Tube Diameter for Single-Wall Carbon Nanotubes. *Phys. Rev. B* **2008**, *77*, No. 241403(R).

(37) Scott, A. P.; Radom, L. Harmonic Vibrational Frequencies: An Evaluation of Hartree-Fock, Möller-Plesset, Quadratic Configuration Interaction, Density Functional Theory, and Semiempirical Scale Factors. *J. Phys. Chem.* **1996**, *100*, 16502–16513.

(38) Baker, J.; Jarzecki, A. A.; Pulay, P. Direct Scaling of Primitive Valence Force Constants: An Alternative Approach to Scaled Quantum Mechanical Force Fields. *J. Phys. Chem. A* **1998**, *102*, 1412–1424.